JOURNAL OF PROPULSION AND POWER
Vol. 17, No. 6, November–December 2001

Computation of a Nonequilibrium Expansion Flow in a Single Expansion Ramp Nozzle

Thomas Link*
University of Technology, D-52062 Aachen, Germany
and
Wolfgang W. Koschel†
DLR German Aerospace Research Center Lampoldshausen, D-74239 Hardthausen, Germany

The simulation of the flow inside the propulsion system is of essential interest, for the design of airbreathing hypersonic vehicles. To compute accurately the expansion flow of a hydrogen/air mixture at high temperatures, the chemical and vibrational nonequilibrium effects must be taken into account. A finite element code is used to model chemical reactions considering finite-rate chemistry and vibrational relaxations according to the Landau–Teller theory (Landau, L., and Teller, E., "Zur Theorie der Schalldispersion," ***Physikalische Zeitschrift der Sowjetunion.*** **Vol. 10, No. 1, 1936, pp. 34–43). The computational domain is discretized by applying unstructured adaptive grids. Different test cases are computed, and the results are compared with measured and numerical data. In one test case, a remarkable difference between the rotational and vibrational temperature of a hydrogen/air nozzle flow is seen. This difference in the experiment is also supported by the computation. Because the applied relaxation rates are small compared to other data given in literature, the thermal nonequilibrium effects gain more importance.**

Nomenclature

c_p	=	specific heat at constant pressure
c_v	=	specific heat at constant volume
e_t	=	specific total energy
e_{rot}	=	specific rotational energy
e_v	=	specific vibrational energy
$\boldsymbol{F}_j$	=	flux vector
h_t	=	specific total enthalpy
$\boldsymbol{H}$	=	vector of source terms
h_t^0	=	heat of formation
$\boldsymbol{I}$	=	identity matrix
$k_{f,r}$	=	forward reaction rate of reaction r
$k_{b,r}$	=	backward reaction rate of reaction r
M_i	=	molar mass of species i
$\boldsymbol{M}$	=	mass matrix
$\boldsymbol{M}_L$	=	lumped mass matrix
N	=	form function
N_r	=	number of reactions
N_{sp}	=	number of species
N_{vsp}	=	number of species with vibrational relaxation
p	=	pressure
$\boldsymbol{q}$	=	heat flux
R	=	specific gas constant
$\Re$	=	universal gas constant
T	=	rotational temperature
T_v	=	vibrational temperature
$\boldsymbol{U}$	=	conserved variables
$\boldsymbol{v}$	=	velocity
X	=	molar fraction
x	=	Cartesian coordinate
Y	=	mass fraction
Γ	=	computational boundary
δ_{ij}	=	Kronecker delta
Θ	=	characteristic vibrational temperature
λ	=	thermal conductivity
μ	=	viscosity
ν	=	Runge–Kutta level
ν', ν''	=	stoichiometric coefficients
ρ	=	density
σ	=	stress tensor
τ	=	relaxation time
Ω	=	computational domain
$\dot{\omega}$	=	chemical production rate

Received 25 June 2000; revision received 26 February 2001; accepted for publication 4 March 2001.

*Research Engineer, Institute for Jet Propulsion and Turbomachinery, RWTH Aachen, Templergraben 55; link@bst.rwth-aachen.de.

†Professor, Institute for Space Propulsion, Langer Grund; wolfgang.koschel@dlr.de. Senior Member AIAA.

Introduction

BECAUSE of a lack of full-scale ground-based test facilities for high-enthalpy flows, the design of airbreathing hypersonic spacecrafts requires efficient and accurate numerical methods. The following results were obtained in a research program that develops computational fluid dynamics (CFD) codes while experimental projects are conducted supplying a database for validation of those codes. The present effort deals with the computation of single expansion ramp nozzle (SERN) flows considering the high-temperature effects of a burning hydrogen/air gas mixture.

Because inlet and exhaust momentum of a hypersonic vehicle are of the same magnitude, the nozzle performance has a strong influence on the net thrust. To predict the nozzle flowfield accurately, it is necessary to consider the physical and chemical effects of high-enthalpy expansion flows. At the beginning of the expansion, a considerable fraction of the combustion products is dissociated. The vibrational degrees of freedom of two and three atom molecules are excited due to the high temperature. During expansion in the nozzle, the velocity of the gas increases and the density decreases rapidly. As a result, the gas molecules are not able to remain in a state of equilibrium because of an insufficient number of collisions. It is known that chemical nonequilibrium should be taken into account for nozzle computation,[1,2] but the importance of thermal nonequilibrium is weighted differently.[1,3] In particular Grønland [1] reported a loss of about 1% of the gross thrust as consequence of thermal nonequilibrium. Because the experimental investigation of a nozzle flow conducted within a complementary project [4] showed a noticeable amount of thermal nonequilibrium, the code was extended to take thermal nonequilibrium effects into account.

Governing Equations

The governing equations are the conservation equations for chemical and thermal nonequilibrium flows. The equations are written in a nondimensional form by introducing the Reynolds number Re, the Mach number M, the Prandtl number Pr, and the Lewis number Le. A Lewis number of unity is assumed, to simplify the calculation of molecular diffusive fluxes.

Continuity equation:

$$\frac{\partial \rho}{\partial t} + \nabla \cdot (\rho \boldsymbol{v}) = 0 \tag{1}$$

Species continuity equation:

$$\frac{\partial (\rho Y_k)}{\partial t} + \nabla \cdot (\rho \boldsymbol{v} Y_k) + \frac{1}{RePr} \nabla \cdot \left(\frac{\lambda}{c_p} \nabla Y_k \right) = w_k \tag{2}$$

Momentum equation:

$$\frac{\partial (\rho \boldsymbol{v})}{\partial t} + \nabla \cdot (\rho \boldsymbol{v}\boldsymbol{v} + p\boldsymbol{I} - \sigma) = 0 \tag{3}$$

with

$$\sigma_{ij} = \mu / Re \left[(\partial_j v_i + \partial_i v_j) - \tfrac{2}{3} (\nabla \cdot \boldsymbol{v}) \delta_{ij} \right] \tag{4}$$

Energy equation:

$$\frac{\partial (\rho e_t)}{\partial t} + \nabla \cdot (\rho \boldsymbol{v} h_t - \sigma \cdot \boldsymbol{v}) + \frac{1}{RePr} \nabla \cdot \boldsymbol{q} = \sum_{k=1}^{N_{\text{vsp}}} -w_{vk} \tag{5}$$

with the heat flux $\boldsymbol{q}$

$$\boldsymbol{q} = -\frac{1}{M^2(\kappa - 1)} \lambda \nabla T - \frac{\lambda}{c_p} \sum_{k=1}^{N_{\text{sp}}} h_k \nabla Y_k \tag{6}$$

Vibrational energy balance:

$$\frac{\partial (\rho Y_k e_{vk})}{\partial t} + \nabla \cdot (\rho Y_k \boldsymbol{v} e_{vk}) = w_{vk} \tag{7}$$

The total energy e_t includes the energy of motion of the gas, the energy of rotational degrees of freedom, and the heat of formation of the molecules

$$e_t = \frac{\boldsymbol{v}}{2} + e_{\text{rot}} + \sum_{k=1}^{N_{\text{sp}}} h^0_{f,k} Y_k \tag{8}$$

with

$$e_{\text{rot}} = \sum_{k=1}^{N_{\text{sp}}} T Y_k c_{\text{vrot}}, k \tag{9}$$

The vibrational energy e_v of an harmonic oscillator is according to Einstein's formula (see Ref. 5)

$$e_v = \frac{\Theta R}{e^{\Theta / T_v} - 1} \tag{10}$$

for molecules of two atoms, and

$$e_v = \frac{\Theta_1 R}{e^{\Theta_1 / T_v} - 1} + \frac{\Theta_2 R}{e^{\Theta_2 / T_v} - 1} + \frac{\Theta_3 R}{e^{\Theta_3 / T_v} - 1} \tag{11}$$

for H_2O. Herein Θ_i are the characteristic vibrational temperatures given in Table 1, and T_v is the vibrational temperature of the molecule or vibrational mode, respectively.

The thermal conductivity λ and the molecular viscosity μ are determined with respect to the temperature and the composition of the gas. The molecular viscosity of pure species is given by

Table 1 Characteristic vibrational temperatures[5]

Molecule	Characteristic vibrational temperatures Θ/K
N_2	3353
$H_2O(\nu 1)$	5260
$H_2O(\nu 2)$	2294
$H_2O(\nu 3)$	5400
H_2	6130
NO	2700

polynomial fits. The viscosity of the mixture is calculated according to Wilke's rule (see Ref. 6)

$$\mu_m(T, X_i) = \sum_{i=1}^{N_{\text{sp}}} \left(\frac{X_i \mu_i}{\sum_{j=1}^{N_{\text{sp}}} X_j \Phi_{ij}} \right) \tag{12}$$

where

$$\Phi_{ij} = \frac{\left[1 + \sqrt{\mu_i / \mu_j \cdot \left(1 / \sqrt{M_i / M_j} \right)} \right]^2}{[8(1 + M_i / M_j)]^{\frac{1}{2}}} \tag{13}$$

Because of the relation between Φ_{ji} and Φ_{ij}

$$\Phi_{ji} = M_i / M_j \cdot 1 / (\mu_i / \mu_j) \cdot \Phi_{ij} \tag{14}$$

only the upper triangle of Φ_{ji} must be determined. Following Reid et al.,[6] the thermal conductivity is computed by

$$\lambda_m(T, X_i) = \frac{1}{\varepsilon} \sum_{i=1}^{N_{\text{sp}}} \left(\frac{X_i \lambda_i}{\sum_{j=1}^{N_{\text{sp}}} X_j \Phi_{ij}} \right), \qquad \varepsilon = 1.065 \tag{15}$$

where Φ of Eq. (13) is used and ε is set to 1.065 (Ref. 7). The equation system is closed by the thermal equation of state

$$p = RT\rho \tag{16}$$

the chemical source terms w_k, and relaxation of vibrational energy w_{vk}, which are described in the next section. When a flow in thermal equilibrium is considered, the balance equation of vibrational energy is neglected and the contribution of vibrational energy is added to the total energy in Eq. (5).

Chemical Source Terms

The chemical source terms w_k are calculated by finite rate chemistry for the species H_2, O_2, H_2O, N_2, NO, OH, N, O, and H. This reaction set was designed for expansion flows of hydrogen and air by Mühleck.[8] The reaction rate of an arbitrary reaction

$$\sum_{k=1}^{N_{\text{sp}}} \nu'_{k,r} B_k \underset{k_b}{\overset{k_f}{\rightleftharpoons}} \sum_{k=1}^{N_{\text{sp}}} \nu''_{k,r} B_k \qquad r = 1, \ldots, N_r \tag{17}$$

is given by

$$\dot{\omega}_r = k_{f,r} \prod_{k=1}^{N_{\text{sp}}} \frac{\rho Y_k}{M_k}^{\nu'_{k,r}} - k_{b,r} \prod_{k=1}^{N_{\text{sp}}} \frac{\rho Y_k}{M_k}^{\nu''_{k,r}} \tag{18}$$

where the forward reaction rate $k_{f,r}$ and the backward reaction rate $k_{b,r}$ are computed according to Arrhenius's law:

$$k_{f,r} = A_{f,r} \cdot T^{n_{f,r}} \cdot \exp(-E_{f,r} / \Re \cdot T) \tag{19}$$

$$k_{b,r} = A_{b,r} \cdot T^{n_{b,r}} \cdot \exp(-E_{b,r} / \Re \cdot T) \tag{20}$$

The parameters A, n, and E are shown in Table 2. The total source term for a specie is given by the summation of the source terms for every reaction, that involves this specie:

$$w_k = \dot{\rho}_k = M_k \sum_{r=1}^{N_r} \left(\nu''_{k,r} - \nu'_{k,r}\right) \cdot \dot{\omega}_r \tag{21}$$

Vibrational Relaxation

A fairly simple model proposed by Pirumov and Roslyakov[5] is used to describe the detailed relaxation mechanism. Pirumov and Roslyakov gave a compilation of vibrational relaxation parameters for expansion flows of various combustion products obtained by experiments. The equations and parameters used in the following section are the processes of their model concerned with combustion products of H_2 in air. The equations are valid for a Boltzmann distribution of the energy and molecules that can be treated as harmonic oscillators. The energy exchange between vibrational and translational energy according to the following processes:

$$N_2 + M \rightleftharpoons N_2^* + M - 2330\,\mathrm{cm}^{-1}$$

$$H_2O + M \rightleftharpoons H_2O^* + M - 1595\,\mathrm{cm}^{-1}$$

$$H_2 + M \rightleftharpoons H_2^* + M - 4260\,\mathrm{cm}^{-1}$$

$$NO + M \rightleftharpoons NO^* + M - 1876\,\mathrm{cm}^{-1}$$

is taken into account. The source terms of these processes are determined by the Landau–Teller theory[9]

$$w_{vk} = \left(e^0_{vk} - e_{vk}\right)\Phi_i \tag{22}$$

where the rate Φ of the ith relaxation process is calculated by

$$\Phi_i = p \sum_{k=1}^{N_{\mathrm{vsp}}} \frac{X_j}{\tau_{ij}} \tag{23}$$

where τ_{ij} is the reaction rate of the jth species in the ith relaxation process. The parameters that are used to compute τ_{ij} are given in Table 3.

Numerical Method

Because of the chemical and vibrational source terms in the conservation equations, the equation system is a so-called stiff system. To solve this stiff system of equations, a semi-implicit method is applied. [10] The employed finite element algorithm is based on the Galerkin weighted-residual method (see Ref. 11). The time integration is achieved by a Runge–Kutta time-marching scheme (see Ref. 12). The weak Galerkin formulation leads to

$$\int_\Omega N\left(\frac{\partial \tilde{U}}{\partial t}\right) \mathrm{d}\Omega = \int_\Omega \frac{\partial N}{\partial x_j}\tilde{\boldsymbol{F}}_j \,\mathrm{d}\Omega \tag{24}$$

$$+ \int_\Omega N\tilde{\boldsymbol{H}}\,\mathrm{d}\Omega - \int_\Gamma N\tilde{\boldsymbol{F}}_j n_j \,\mathrm{d}\Gamma \tag{25}$$

where the conservative variables U, the fluxes F_j, and the source terms H are represented by a C^0 linear approximation:

$$\tilde{U} = \sum_K N_K \boldsymbol{U}_K \tag{26}$$

where U_K denotes the nodal values of U. The spatial integration of Eq. (24) results in

$$\boldsymbol{M}\frac{\partial \boldsymbol{U}}{\partial t} = \boldsymbol{R}_j(\boldsymbol{F}_j) + \boldsymbol{M}\boldsymbol{H} \tag{27}$$

In the semi-implicit procedure the source terms are determined at the time $n+1$, whereas the flux terms are computed at the time n

$$\boldsymbol{M}\frac{\partial \boldsymbol{U}}{\partial t} = \boldsymbol{R}\left(\boldsymbol{F}_j^n\right) + \boldsymbol{M}\boldsymbol{H}^{n+1} \tag{28}$$

The linearization of the source terms

$$\boldsymbol{H}^{n+1} = \boldsymbol{H}^n + \frac{\partial \boldsymbol{H}}{\partial \boldsymbol{U}}\Delta \boldsymbol{U} \tag{29}$$

and substitution of the time derivation by a Taylor series yields the scaled equation

$$\boldsymbol{M}\left(\boldsymbol{I} - \Delta t\frac{\partial \boldsymbol{H}}{\partial \boldsymbol{U}}\right)\frac{\Delta \boldsymbol{U}}{\Delta t} = \boldsymbol{R}_j\left(\boldsymbol{F}_j^n\right) + \boldsymbol{M}\boldsymbol{H}^n \tag{30}$$

Table 2 Finite-rate chemistry[8]

No.	Reaction	A_f	n_f	$E_f/\Re$	A_b	n_b	$E_b/\Re$
1	$H + H + M \rightleftharpoons H_2 + M$	$6.4e17$	-1	0	$5.5e18$	-1	51,987
2	$O + O + M \rightleftharpoons O_2 + M$	$6.0e13$	0	-503.3	$7.2e18$	-1	59,340
3	$H + O_2 \rightleftharpoons OH + O$	$2.2e14$	0	8,455	$1.5e13$	0	0
4	$H_2 + O \rightleftharpoons OH + H$	$1.8e10$	1	4,479	$3.0e13$	0	4,429
5	$OH + H_2 \rightleftharpoons H_2O + H$	$2.2e13$	0	2,592	$8.4e13$	0	10,116
6	$H_2O + M \rightleftharpoons H + OH + M$	$5.2e21$	-1.5	59,386	$2.2e22$	-2	0
7	$O + H + M \rightleftharpoons OH + M$	$7.1e18$	-1	0	$8.5e18$	-1	50,830
8	$H_2O + O \rightleftharpoons OH + OH$	$5.8e13$	0	9,059	$6.3e12$	0	549
9	$H_2 + O_2 \rightleftharpoons OH + OH$	$1.7e13$	0	24,232	$5.7e11$	0	14,922
10	$N + O_2 \rightleftharpoons NO + O$	$6.4e9$	1	3,170	$2.4e11$	0.5	19,200
11	$N + NO \rightleftharpoons N_2 + O$	$1.6e13$	0	0	$5.0e13$	0	37,940
12	$N + OH \rightleftharpoons NO + H$	$4.5e13$	0	0	$1.7e14$	0	24,500

[a]Units are mole, caloric, second, Kelvin, and cubic centimeter. Third-body efficiencies for reaction 1 are 2 for H_2 and 6 for H_2O, for reaction 6 are 6 for H_2O, and for reaction 7 are 5 for H_2O.

Table 3 Relaxation time[5]

	$\ln\tau/\ln(\mathrm{atm}\cdot\mathrm{s})$ of process			
Molecule	1	2	3	4
N_2	$220T^{-1/3}-24.81$	$-36.8T^{-1/3}-10.85$	$100T^{-1/3}-20.3$	$100T^{-1/3}-18.3$
H_2O	$33.5T^{-1/3}-16.55$	$-36.8T^{-1/3}-13.15$	$100T^{-1/3}-21.67$	$100T^{-1/3}-18.3$
H_2	$86.9T^{-1/3}-19.94$	$-36.8T^{-1/3}-10.85$	$100T^{-1/3}-21.67$	$100T^{-1/3}-18.3$
NO	$223.9T^{-1/3}-24.96$	$-36.8T^{-1/3}-10.85$	$100T^{-1/3}-20.3$	-14.9

The integration in time is performed by a Runge–Kutta scheme applied to every node K

$$\boldsymbol{U}_K^{(\nu+1)} = \boldsymbol{U}_K^n + \boldsymbol{S}^{-1}\alpha_\nu \Delta t_K \left[\boldsymbol{M}_L^{-1}\boldsymbol{R}\left(\boldsymbol{U}_K^{(\nu)}\right) + \boldsymbol{H}_K^\nu + \left(\boldsymbol{D}_K^{(2)} - \boldsymbol{D}_K^{(4)}\right)\right]$$

$$\boldsymbol{U}_K^{n+1} = \boldsymbol{U}_K^{(5)} \qquad \nu = 0, \cdots, 4 \tag{31}$$

In Eq. (31), a local time step Δt_k is used, the element mass matrix $\boldsymbol{M}$ is replaced by the lumped mass matrix $\boldsymbol{M}_L$, and $\boldsymbol{S}$ denotes $\boldsymbol{I} - \Delta t\,(\partial \boldsymbol{H}/\partial \boldsymbol{U})$.

Artifical viscosity is added to the scheme by the damping terms $\boldsymbol{D}_K^{(2)}$ and $\boldsymbol{D}_K^{(4)}$. The term $\boldsymbol{D}_K^{(2)}$ represents the nodal value of a nonlinear shock-capturing term[13]:

$$\boldsymbol{D}_K^{(2)} = c_d^{(2)} \boldsymbol{M}_L^{-1} \sum_e \frac{S_e}{\Delta t_e} (\boldsymbol{M} - \boldsymbol{M}_L)\boldsymbol{U}^{n+1} \tag{32}$$

where S_e and Δt_e are elemental averaged values and $c_d^{(2)}$ denotes a constant diffusion coefficient. The nodal quantity S_I is given by

$$S_I = \left| \sum_e \frac{(\boldsymbol{M} - \boldsymbol{M}_L)p}{|(\boldsymbol{M} - \boldsymbol{M}_L)p|} \right| \tag{33}$$

scaled from zero in smooth flow regions to one near discontinuities.

$\boldsymbol{D}_K^{(4)}$ denotes a linear fourth-order, high-frequency damping term also given by Morgan and Peraire,[13]

$$\boldsymbol{D}_K^{(4)} = \boldsymbol{M}_L^{-1} \sum_e \frac{\chi^{(4)}}{\Delta t_e} (\boldsymbol{M} - \boldsymbol{M}_L) \left[\boldsymbol{M}_L^{-1} \sum_e (\boldsymbol{M} - \boldsymbol{M}_L)\boldsymbol{U} \right] \tag{34}$$

To reduce overshoots near shock waves, strong contributions of $\boldsymbol{D}_K^{(4)}$ are suppressed by defining

$$\chi^{(4)} = \max\left(0, c_d^{(4)} - c_d^{(2)} S_e\right) \tag{35}$$

with $c_d^{(4)}$ as a user-specified constant.

Boundary Conditions

The convective fluxes within the boundary integral of Eq. (24) are corrected by use of a linearized characteristics analysis. Along walls without friction, the velocity is set tangential to the wall and otherwise to zero.[11]

Mesh Generation

The described numerical method is well suited to work with unstructured meshes and reaches an accuracy of second order.[13] The discretization for arbitrarily shaped computational domains is accomplished by an automatic mesh generation scheme following the generalized advancing-front method.[14] Points and elements are generated simultaneously and, therefore, significant changes in the local mesh structure are possible. On the surface of bodies, rectangular elements are used to provide an efficient discretization of the boundary layer, whereas the remaining part of the domain is discretized by unstructured triangular elements.

The automatic mesh generation scheme offers the ability to improve the solution by remeshing the computational domain. To determine the nodal values of the mesh parameters in an optimal manner, it is necessary to apply a method of error estimation. Therefore, the form function of a finite element is treated as a Lagrange polynomial. It is possible to determine the interpolation error between an arbitrary twice differentiable function and a Lagrange polynomial. This leads to an expression that depends on the second derivative of a scalar key variable, for example density, pressure, or Mach number. The optimized nodal values of the mesh parameters are achieved when the interpolation error is uniformly distributed within the computational domain.

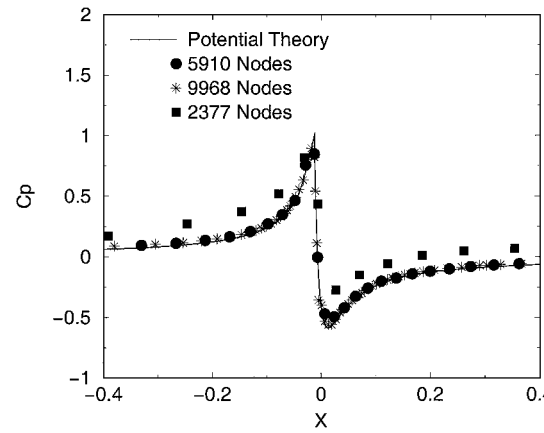

Fig. 1 Comparison between different refined grids and the theoretical solution.

The remeshing procedure starts generally with a coarse grid. After computation of the solution on this grid, the grid is refined, and the next computation cycle is started. During the refinement, the computational mesh that was used to compute the present solution is now acting as a background grid providing the spatial distribution of the mesh parameters. This refinement is applied repeatedly until the solution is not altered due to a finer grid. An example for this procedure is shown in Fig. 1. The code was used to compute a potential flow around a semi-infinite half-body (superposition of uniform flow and a source).[15] The width of the body for $x \to \infty$ is 0.04 m and the Mach number of the freestream is $Ma = 0.2$. In Fig. 1 the results for

$$c_p = \frac{p - p_\infty}{\rho_\infty \left(v_\infty^2/2\right)} \tag{36}$$

on a symmetrical streamline and the body surface are plotted vs the longitudinal coordinate. The solid line is the solution given by the theory of potential flows. The symbols are the computed solution with a grid of 2377, 5910, and 9968 nodes. For graphical clarity every third point is shown. It is obvious that the solution is improved by the first remeshing. The results of the second mesh are nearly grid independent because they are in good agreement with the theory and a further remeshing does not improve the solution.

Computational Results

First, two test cases for nonequilibrium nozzle flows taken from literature were studied and compared to the computational results of the present work. In a second step, the reactive flow of a SERN nozzle in thermal nonequilibrium was numerically simulated and compared to experimental results.

Nozzle Flow in Chemical Nonequilibrium

For the validation of the finite-rate chemistry model, a nozzle flow of a stoichiometric hydrogen/air mixture that was numerically investigated by Walther [16] is computed. The two-dimensional converging–diverging nozzle consists of a plain and a curved wall. The shape of the nozzle and the computed Mach number distribution are shown in Fig. 2. The area ratio is 13.9, and the total length 12.3 m. Walther performed a two-dimensional Euler calculation using a finite-rate chemistry model and Moretti's λ scheme. As boundary conditions, at the inlet, a total temperature of 2780 K and a total pressure of 8 bar were taken. In Figs. 3 and 4 the composition along the curved wall of Walther's computation is compared to the results of the present solver at the same conditions. The comparison shows a good agreement for the species H_2, O_2, H_2O, and OH. The differences between the mass fractions of H and O is due to Walther's reduced finite-rate chemistry model. He used only six reactions for the H_2/air system. In particular reactions 1 and 2 in Table 2 are neglected. Three-body reactions provide the possibility

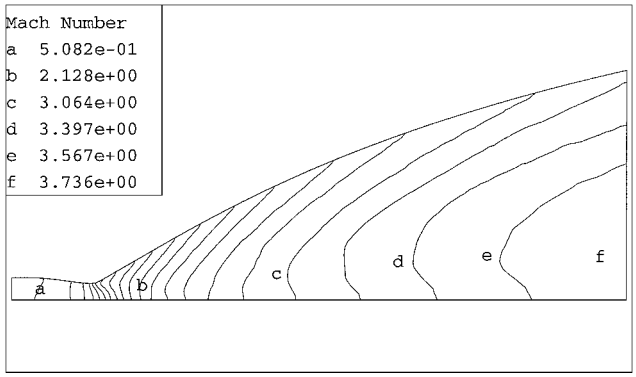

Fig. 2 Computed Mach number distribution of Walther's[16] nozzle.

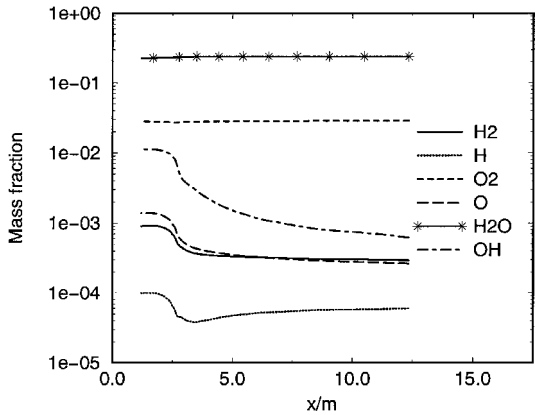

Fig. 3 Computed composition along the curved wall of Walther's[16] nozzle.

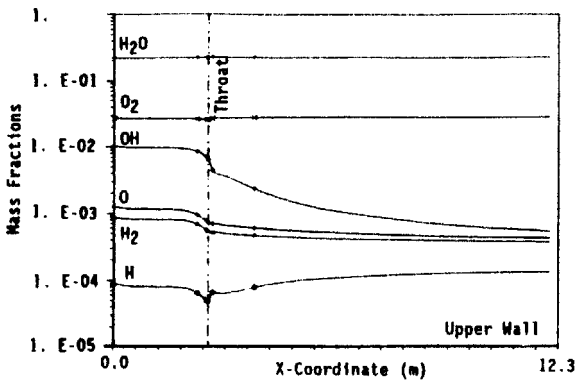

Fig. 4 Composition reported by Walther.[16]

of recombination of H and O and lead to a smaller mass fraction of these species.

Nozzle Flow in Thermal Nonequilibrium

A test case for flows in thermal nonequilibrium was published by Sharma et al.[17] In their studies, the flow of purified N_2 in a planar and symmetrical nozzle was experimentally and numerically investigated. The converging–diverging nozzle had a total length of 10.8 cm and an area ratio of 11.7. The conditions at the inflow boundary are a total temperature of 2800 K and a total pressure of 103.6 bar. For validation purposes, the flow in the nozzle is computed by the presented solver including the finite-rate chemistry model and the thermal nonequilibrium model. The allowed impurities of 10 ppm are arbitrary distributed among the other species of the H_2/air system. The nozzle shape and computational results of vibrational temperature and Mach number are shown in Fig. 5. The upper contour plot in Fig. 5 is the vibrational temperature with a spacing of about 30 K between the lines. The lower part is the

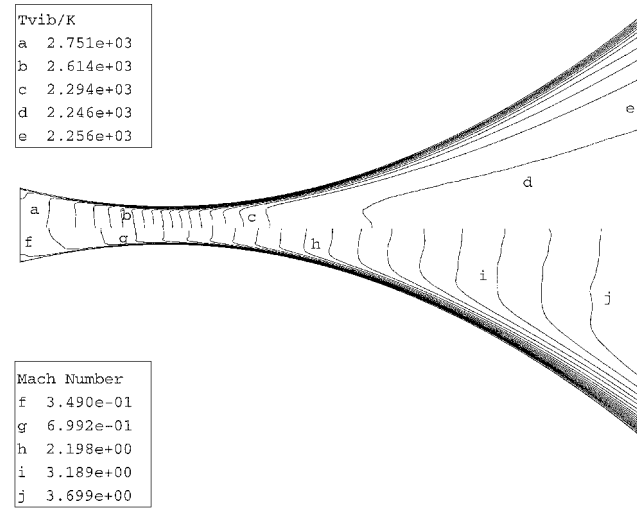

Fig. 5 Upper part: computed contour plot of vibrational temperature; lower part: computed contour plot of Mach number of Gillespie and Sharma's nozzle flow.[18]

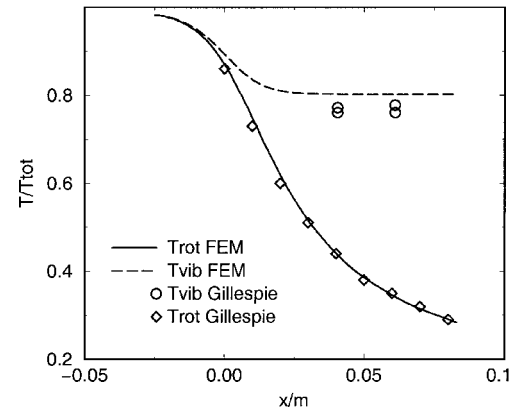

Fig. 6 Computed vibrational and rotational temperature on the centerline of the nozzle compared with data published by Gillespie and Sharma.[18]

Mach number with a spacing of about 0.2. The computed rotational/translational and vibrational temperatures on the centerline of the nozzle are compared with the data reported by Gillespie and Sharma[18] in Fig. 6. Gillespie and Sharma's data of the vibrational temperature are measured by a method using spontaneous Raman scattering, whereas the rotational/translational temperature are samples of numerical results. The rotational/translational temperatures in Fig. 6 are in good agreement. The measured vibrational temperature is hardly lower than the computed one, but this tendency can be seen in Gillespie and Sharma's numerical results as well.

Numerical Investigation of a Reactive SERN Nozzle Flow in Thermal Nonequilibrium

The experiment was performed by Weisgerber and Fischer[4] and Weisgerber et al.[19] at the DLR, German Aerospace Research Center, Cologne. The nozzle flow was investigated by wall pressure measurement and temperature probes in the nozzle wall. At the outlet of the SERN nozzle, the profile of velocity was measured by a laser-2-focus (L2F) system, and the profile of rotational and vibrational temperature of the N_2 molecule was obtained by coherent anti-Stokes Raman scattering measurements. At the inlet of the nozzle, the same measurements were used; however, due to beam distortion, the examination of velocity and temperature was only possible in the middle of the inlet cross section. A matrix burner was used to provide a uniform mixture of combustion products of hydrogen/air combustion at the nozzle inlet. Because of the high total temperature of the combustion products, the nozzle walls had

to be cooled. Because of insufficient experimental data for the nozzle inlet, some assumptions are necessary to determine the inlet conditions for the computation. It is assumed that the total pressure and the total temperature are constant in the inlet cross section and that the boundary-layer thickness is negligible. The composition of the gas at the inlet was not analyzed in the experiment. Therefore, it is assumed to be equal to the composition in chemical equilibrium. The boundary conditions that are used in the computations are given in Table 4.

The nozzle flow is computed by solving the Navier–Stokes equations for chemically reacting flow in thermal nonequilibrium. The turbulence in the boundary layer is modeled by a Baldwin–Lomax turbulence model (see Ref. 20). The pressure at the nozzle outlet is fitted in such a way that the flow in the boundary layer does not separate. The computational grid that is used is shown in Fig. 7. The computed Mach number distribution, as shown in Fig. 8, illustrates that the measuring flange that is mounted at the end of the nozzle generates a shock due to the sharp bend of the wall.

The influence of the chemical reactions are shown in Figs. 9 and 10. As shows in Fig. 10, the radical OH decreases strongly throughout the nozzle while H increases slightly. This behavior is often detected in nozzle flows.[1,16] According to Grønland,[1] the increasing H mass fraction is a consequence of the decreasing number density that results in slower three-body reactions.

The comparison between the measured and the computed wall pressures in Fig. 11 shows excellent agreement. In Fig. 12, the measured and calculated temperature profiles of rotational/translational and vibrational temperature at the nozzle exit are shown. The difference between the rotational/translational and vibrational temperature at the exit is remarkable because of the high water content in the

Table 4 Inlet boundary conditions

Condition	Value
Mass fraction	
H_2	$0.598e-3$
H	$0.154e-4$
O_2	$0.266e-2$
O	$0.692e-4$
H_2O	0.248
OH	$0.219e-2$
N	$0.128e-7$
NO	$0.212e-2$
N_2	0.744
Total temperature T_t, K	2376 k
Total pressure p_t, Pa	$11e5$

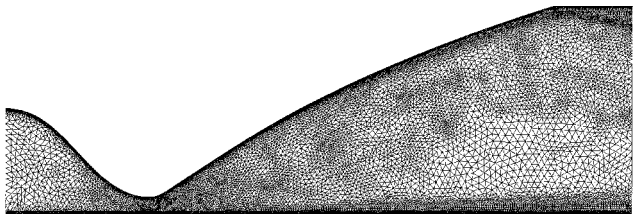

Fig. 7 Computational grid.

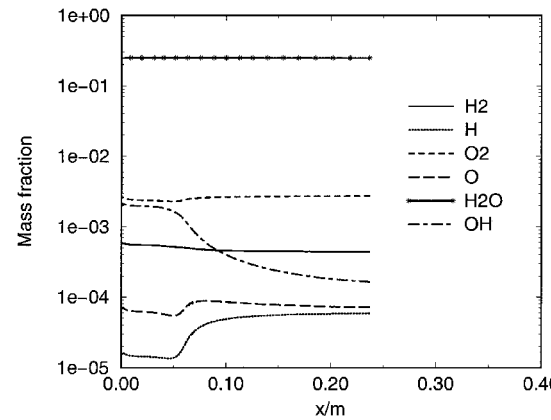

Fig. 10 Computed composition in the middle of the nozzle vs nozzle length.

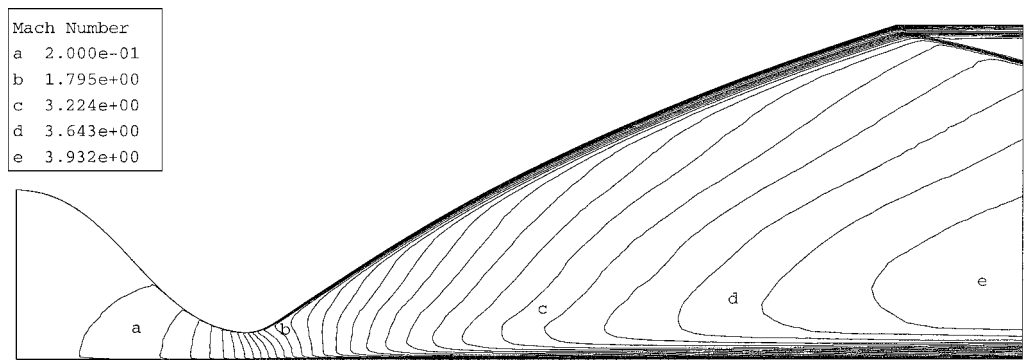

Fig. 8 Computed Mach number distribution.

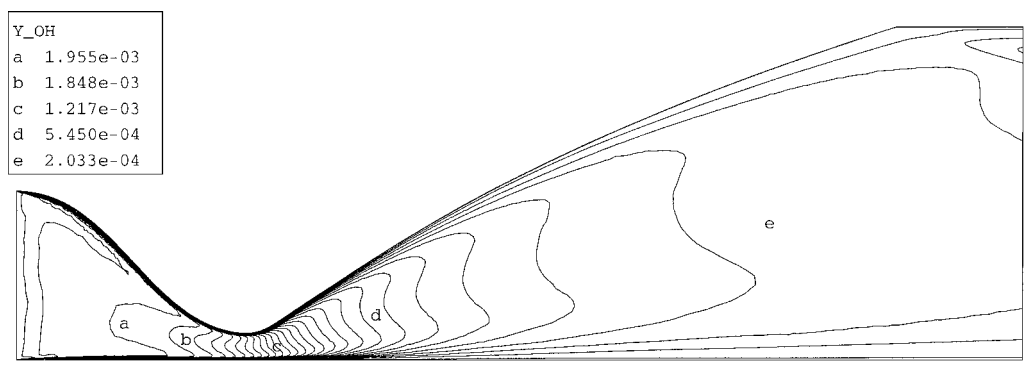

Fig. 9 Computed contour plot of OH mass fraction.

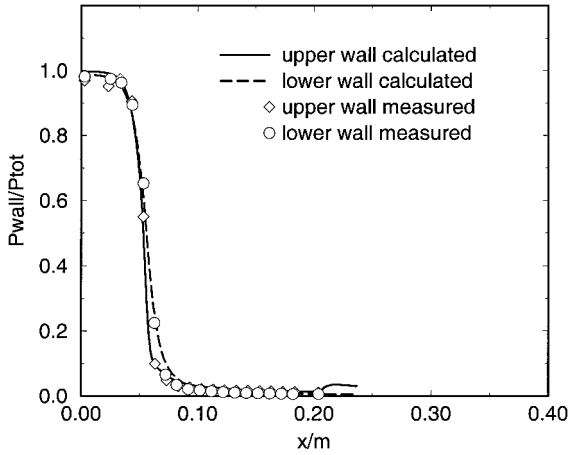

Fig. 11 Computed and measured pressures along the wall.

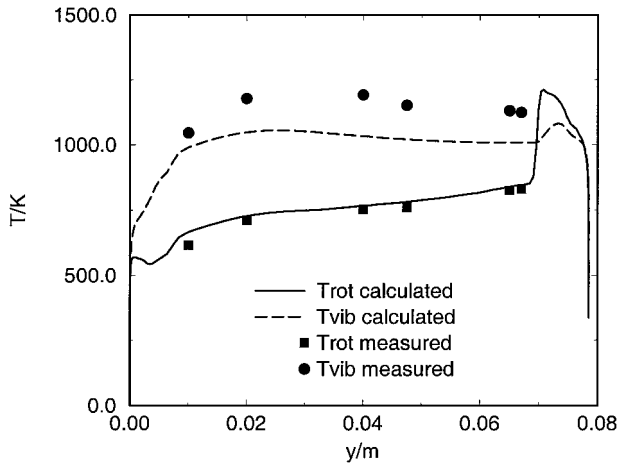

Fig. 12 Computed and measured profile of rotational and vibrational temperatures of N_2 molecules at the outlet of the nozzle.

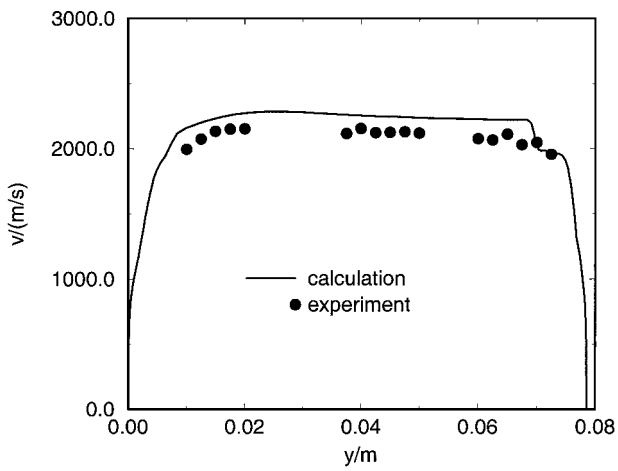

Fig. 13 Computed and measured velocity profile at the outlet of the nozzle.

gas. Water is known as very effective for deexcitation of the excited N_2 molecules. The drop of the temperatures in the vicinity of the walls is a consequence of the cooling, whereas the sharp rise of the rotational/translational temperature at $y \approx 0.07$ m is a result of the shock in the flowfield. The computed rotational/translational temperature profile agrees very well with the measurement. The comparison between measured and calculated vibrational temperatures show a about 10% lower temperature in the computation. The relaxation of N_2 in the mixture is obviously overestimated, but if Pirumov and Roslyakov's[5] relaxation rate is compared with other data in the literature, often an even larger deexcitation of the N_2 molecule is found.[21]

In Fig. 13, the velocity profiles at the nozzle exit are shown. The computed velocities are about 5% higher than the measured one, but the shape of measured and computed profiles and, thus, the boundary-layer thickness are equal. One reason for this difference of the velocities is the experimental error. Because of the slippage of the particles that are needed for the L2F measurements, the error of measurement is about 1.5% (Ref. 19). The remaining error is inexplainable and may be a result of the incomplete boundary conditions at the nozzle inlet.

Conclusions

A flow solver on unstructured grids for a chemical and thermal nonequilibrium is presented. The validation of the code was done for two test cases published in the literature. Then a basic nozzle experiment was computed and compared to the measured results. With respect to the available experimental data, the computed and measured results are in good agreement. Although state-of-the-art measurements were used to investigate the experimental configuration, it was not possible to examine the flow in all details. In particular, detailed information about the nozzle inlet and the composition in the nozzle flowfield would be valuable for the code validation. The difficulties encountered during the experimental investigation show the need of further experiments for CFD validation. Nevertheless, the computation of SERN nozzles of realistic length can be performed by the present code with a satisfying accuracy to estimate the thrust losses caused by thermal nonequilibrium.

Acknowledgment

The authors acknowledge the financial support of this work by the Deutsche Forschungsgemeinschaft within the framework of the Sonderforschungsbereich 253 at RWTH Aachen.

References

[1]Grønland, T. A., and Cambier, J. L., "Sensitivity to Physical Modeling for Nozzle/Afterbody Flowfields," AIAA Paper 96-4547, April 1996.

[2]Sangiovanni, J. J., and Barber, T. J., "Role of Hydrogen/Air Chemistry in Nozzle Performance for a Hypersonic Propulsion System," *Journal of Propulsion and Power*, Vol. 9, No. 2, 1993, pp. 134–138.

[3]Rizkalla, O., Chinitz, W., and Erdos, J. I., "Calculated Chemical and Vibrational Nonequilibrium Effects in Hypersonic Nozzles," *Journal of Propulsion and Power*, Vol. 6, No. 1, 1990, pp. 50–57.

[4]Weisgerber, H., and Fischer, M., "Experimentelle Untersuchung zur Expansionsströmung nach Wasserstoff/Luft-Verbrennung in luftatmenden Hyperschallantrieben," Deutsches Zentrum für Luft- und Raumfahrt, Rept. DLR-IB-325-04-97, April. 1997.

[5]Pirumov, U. G., and Roslyakov, G. S., *Gas Flow in Nozzles*, Springer, Berlin, 1986, pp. 231–248.

[6]Reid, C. R., Prausnitz, J. M., and Poling, B. E., *The Properties of Gases and Fluids*, 4th ed., McGraw–Hill, New York, 1987, pp. 530–535.

[7]Mason, E. A., and Saxena, S. C., "Approximate Formula for the Thermal Conductivity of Gas Mixtures," *Physics of Fluids*, Vol. 1, No. 5, 1958, pp. 361–369.

[8]Mühleck, P., "Numerische Untersuchung turbulenter reagierender Strömungen in Brennkammern und Schubdüsen von Hyperschall-Staustrahltriebwerken," Deutsches Zentrum für Luft- und Raumfahrt, Rept. DLR-FB 95-10, 1995.

[9]Landau, L., and Teller, E., "Zur Theorie der Schalldispersion," *Physikalische Zeitschrift der Sowjetunion*, Vol. 10, No. 1, 1936, pp. 34–43.

[10]Bussing, T. R. A., "A Finite Volume Method for the Navier–Stokes Equations with Finite Rate Chemistry," Dept. of Aeronautics and Astronautics, Massachusetts Inst. of Technology, Cambridge, MA, 1985.

[11]Rick, W., "Adaptive Galerkin Finite Elemente Verfahren zur numerischen Strömungssimulation auf unstrukturierten Netzen," Dissertation, Inst. für Strahlantriebe, RWTH Aachen, Germany, 1994.

[12]Mavripilis, D. J., "Accurate Multigrid Solution of the Euler Equations on Unstructured and Adaptive Meshes," *AIAA Journal*, Vol. 28, No. 2, 1990, pp. 213–221.

[13]Morgan, K., and Peraire, J., "Finite Element Methods for Compressible Flows," Lecture Series for Fluid Dynamics, von Kármán Inst., Rhode-St. Genese, The Netherlands, 1987.

[14]Bikker, S., Greza, H., and Koschel, W., "Parallel Computing and Multigrid Solution on Adaptive Unstructured Meshes," *Notes on Numerical Fluid Mechanics*, edited by F.-K. Hebeker, Vol. 47, Vieweg, Brunswick, Germany, pp. 148–154.

[15]Anderson, J. D., *Fundamentals of Aerodynamics*, McGraw–Hill, 2nd ed., New York, 1991, pp. 189–191

[16]Walther, R., "Numerical Analysis of Converging-Diverging Nozzle Flow in Chemical Nonequilibrium," AGARD Symposium of CFD-Techniques for Propulsion Applications, Paper No. 44, Feb. 1992.

[17]Sharma, S. P., Ruffin, S. M., Gillespie, W. D., and Meyer, S. A., "Vibrational Relaxation Measurements in an Expanding Flow Using Spontaneous Raman Scattering," *Journal of Thermophysics and Heat Transfer*, Vol. 7, No. 4, 1993, pp. 697–703.

[18]Gillespie, W. D., and Sharma, S. P., "Raman Scattering Measurements of Vibrational Relaxation in Expanding Nitrogen," *Shock Waves at Marseille*, edited by R. Brun, Vol. 2, Springer, Berlin, 1995, pp. 229–234.

[19]Weisgerber, H., Fischer, M., Magens, E., Winandy, A., Förster, W., and Beversdorff, M., "Experimental Analysis of the Flow of Exhaust Gas in a Hypersonic Nozzle," AIAA Paper 98-1600, April 1998.

[20]Bikker, S., "Beitrag zur Strömungssimulation auf Hochleistungsrechnern mit Finite Elemente Methoden," Dissertation, Inst. für Strahlantriebe, RWTH Aachen, Germany, 1996.

[21]Weisgerber, H., Fischer, M., Magens, Beversdorff, M., Link, T., and Koschel, W., "Experimental and Numerical Analysis of an Expansion Flow in Chemical and Thermal Nonequilibrium," *Proceedings of the Fourteenth International Symposium on Airbreathing Engines*, ISABE Paper 99-7134, Sept. 1999.